NANO LETTERS
Letter
pubs.acs.org/NanoLett

Direct-Bandgap Epitaxial Core−Multishell Nanopillar Photovoltaics Featuring Subwavelength Optical Concentrators

Giacomo Mariani,*,[†] Zhengliu Zhou,[‡] Adam Scofield,[†] and Diana L. Huffaker[†,§]

[†]Electrical Engineering Department, University of California at Los Angeles, Los Angeles, California 90095, United States
[‡]Mechanical and Aerospace Engineering Department, University of California at Los Angeles, Los Angeles, California 90095, United States
[§]California NanoSystems Institute, University of California at Los Angeles, Los Angeles, California 90095, United States

Supporting Information

ABSTRACT: Semiconductor nanomaterials have recently fueled numerous photonic scientific fields. Arrays of nanopillars (NPs) have been examined by the photovoltaic (PV) community as highly efficient solar absorbers, with potential material/cost reductions compared to planar architectures. Despite modeled predictions, experimental efficiencies are limited by surface recombination and poor light management, once integrated in a practical PV device. In this Letter, we correlate optoelectronic modeling with experimental results for direct-bandgap arrays of core-multishell GaAs NPs grown by selective area, catalyst-free epitaxy and capped by epitaxial window layers, with efficiencies of 7.43%. Electrically, improved open-circuit voltages are yet partly affected by residual surface state density after epitaxial passivation. Optically, dome-shaped indium−tin−oxide (ITO) top electrode functions as a two-dimensional (2-D) periodic array of subwavelength lenses that focus the local density of optical states within the NP active volume. These devices provide a path to high-efficiency NP-based PVs by synergistically controlling the heteroepitaxy and light management of the final structure.

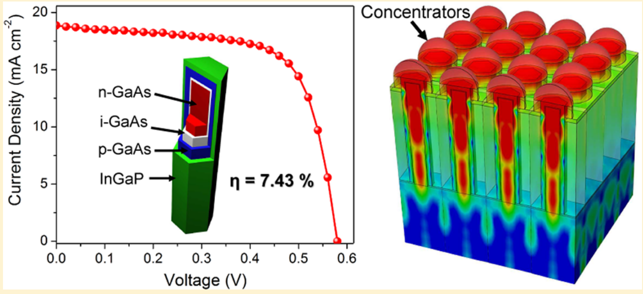

KEYWORDS: *Nanowire, solar cell, core−shell, ITO, concentrator, passivation, GaAs, nanopillar, dome*

Nanomaterials and nanopillar (NP) photonics has recently enabled advances in several research fields including optical modulators,[1] light-emitting sources,[1,2] photodetectors,[3−5] and solar cells.[6−9] Semiconductor NPs have exhibited exciting (1) optical properties in terms of tunability and enhanced absorption[10] and (2) electrical properties of radial junctions in terms of charge separation more tolerant to material defects.[11] For these reasons, a considerable body of literature is exploiting NPs as next-generation photovoltaic elements. Nanometer-sized footprint of NPs allows for a dissimilar material integration, where lattice matching requirements due to strain accommodation are relaxed. For instance, silicon nanowires (NWs) can be grown on a wide variety of substrates[12] and also direct-bandgap III−V NPs can be synthesized on inexpensive platforms.[13,14] In addition, the NPs can be released from the native substrate and integrated into flexible,[15] low-cost photovoltaic devices.

To analyze the interaction of a normally incident optical field with semiconducting NPs, single-NW devices are generally fabricated by dispersing the nanostructures onto an oxide-coated silicon substrate. Previous works demonstrated optical absorption engineering through leaky-mode resonances[10] arising from the subwavelength confinement of light. Furthermore, polarization-resolved external quantum efficiency (EQE) spectra exhibited diameter-dependent peaks, tunable by a morphological design of the structures.[7] However, the strength of NP photovoltaics manifests when arrays of three-dimensional (3-D), vertically aligned NPs are considered collectively: light trapping increases the effective optical path-length of the incoming photons, exceeding the $2n^2$ Lambertian limit under certain conditions.[16] This effect enhances considerably the absorption of solar radiation with respect to planar architectures. The adoption of a periodic, position-controlled NP array can be employed to tune the corresponding absorption properties. Specific values, such as diameter (D) and pitch (P), can strongly affect the propagation of light in the subwavelength regime,[17] where the sequence of high refractive index III−V material and air can be formalized by the effective medium approximation theory.

Direct-bandgap III−V compounds benefit from extremely high optical absorption coefficients, resulting into ∼100 times thinner material required to absorb 90% of above-bandgap solar photons[11] compared to silicon. Furthermore, a rigorous analysis of several III−V semiconductors including InP,[18] InAs,[19] and GaAs[17] NP arrays report wideband absorption values

Received: January 8, 2013
Revised: February 22, 2013
Published: March 13, 2013

dx.doi.org/10.1021/nl400083g | *Nano Lett.* 2013, 13, 1632−1637

approaching unity. Nonetheless, photon-to-electron power conversion efficiencies (PCEs) of NP-array photovoltaics based on this class of materials remain limited to 3.37%,[6] under air mass 1.5 global (AM1.5G). Hence, it becomes necessary to intimately correlate the optical properties of the fully integrated device structure (that will interface to the external optical field) with the electrical properties of the NP solar cell measured at the terminals. In this work, we directly correlate finite-difference time domain (FDTD) simulations with current−voltage ($J-V$) and EQE experimental data of GaAs p−i−n core−multishell NP solar cells capped with InGaP window shells, with a measured AM1.5G PCE of 7.43%. The analysis highlights a residual surface state density after epitaxial passivation and an appreciable optical focusing effect arising from dome-shaped indium−tin−oxide (ITO) layer that intensifies and concentrates the optical field within the NP (see Supporting Information). At short wavelengths, the lens-like behavior is localized at the NP tip, whereas at longer wavelengths the light field penetrates deeper, yet confined into the nanostructure.

The GaAs NP solar cells consist of a core−multishell structure as shown in the schematic of Figure 1a. The NPs are grown by means of selective-area metal organic chemical vapor deposition, without any metal catalyst to foster the synthesis that could affect the device performance. The details on the masking and growth conditions are reported elsewhere.[20] In brief, a Sn-doped GaAs n-core ($N_D \sim 1 \times 10^{17}$ cm^{-3}, from planar calibrations) with 180 nm diameter is first grown. Second, a ~10 nm intrinsic GaAs shell followed by a 40 nm Zn-doped GaAs p-shell ($N_A \sim 3 \times 10^{18}$ cm^{-3}) are formed. Lastly, a ~5 nm InGaP window layer is synthesized to mitigate NP surface recombination.[21] This is carried out by a careful control of the heteroepitaxy in the NP in terms of temperature and flow rates during growth. The final core−multishell NP height and diameter are 1.3 μm and ~290 nm, respectively. Figure 1b shows a scanning electron microscopy (SEM) picture of a typical array growth. The NPs are hexagonally faceted, arranged in a square tiling pattern. Ratios of $D/P \sim 0.5$[17] are shown to maximize the absorption in periodic GaAs NP arrays; therefore a pitch of 600 nm is chosen here. Subsequent to epitaxy, benzocyclobutene (BCB) is used to planarize the NP array and, after hard curing, etched back to expose ~350 nm tips. Figure 1c displays the partly exposed NPs. On the right half of the figure, a 80 degree-tilted SEM picture is provided: to notice the low variability in height, witnessing fairly constant growth rates for the NPs across the device.

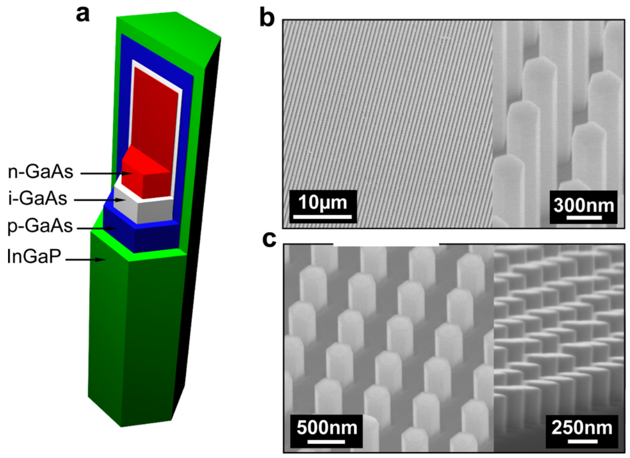

Figure 1. (a) 3-D illustration of the designed/fabricated nanopillar (NP) core-multishell structure: the p−i−n radial junction is wrapped in InGaP shell to lessen surface-state-induced surface recombination. (b) Typical scanning electron microscope (SEM) image of vertically aligned NP arrays. (c) BCB planarization layer and etch-back step to partly expose back the NP.

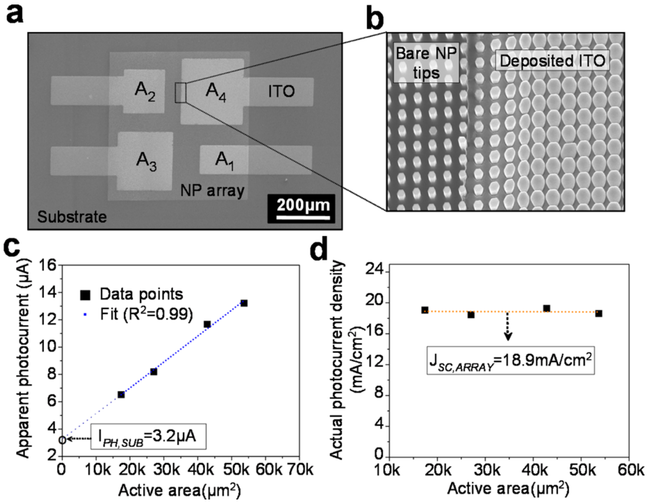

Figure 2. (a) Top-view SEM image of a NP array with four area-dependent transparent contacts photolithographically defined on top. (b) SEM micrograph of the zoomed-in boundary in a. To notice the difference between bare NP tips and conformal dome-shaped morphology once ITO is deposited. (c) Apparent photocurrent/active area characteristics for NP solar cells with increasing area. The extrapolated substrate photocurrent from the linear regression (R^2 = 0.99) is 3.2 μA. (d) Actual photocurrent density/active area plot showing a 18.9 mA/cm^2 current density irrespective of the device area.

Photocurrent spectroscopy measurements on doped-GaAs homoepitaxial layers have shown photocurrent contributions resulting from illuminating the semiconductor.[22] An estimated minority carrier diffusion length between ~0.4 and ~2 μm[22,23] has been extrapolated for layers at different doping concentrations. Therefore, it becomes necessary to rule out possible photocurrents generated in the substrate ($I_{PH,SUB}$) that could be recollected by the NP arrays, measuring a higher apparent short-circuit current density ($J_{SC,APP}$) given by

$$J_{SC,APP} = \frac{I_{PH,SUB}(V = 0) + I_{PH,ARRAY}(V = 0)}{\text{active array area}}$$

where $I_{PH,ARRAY}$ represents the actual photocurrent solely output by the NP-array solar cell. To separate the two addends, an area-dependent measurement is required. Each NP-array photovoltaic device, in fact, is grown on a cleaved 1 cm × 1 cm n-doped GaAs substrate, wherein a NP subregion is defined as active area. For this reason, a 0.5 mm × 0.5 mm active array area is defined. Figure 2a presents a top-view SEM picture where four different transparent electrodes with increasing areas are contacting the NP-array: A_1, A_2, A_3, and A_4 correspond to NP-areas of 14410, 27030, 42830, and 53700 μm^2, respectively. The probing pads that extend outside the active regions are electrically isolated from the substrate by the BCB resin. Figure 2b displays a contact boundary between the bare NP tips after the planarization process and the sputtered contact that forms a dome-shaped ITO electrode. The

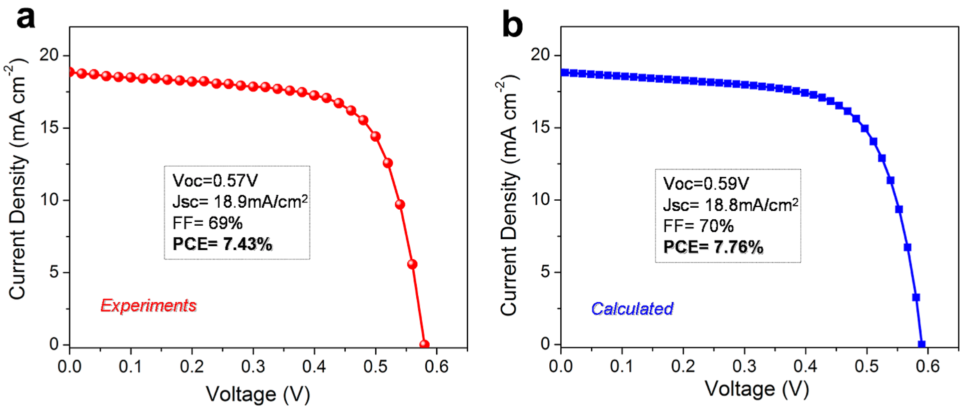

Figure 3. (a) Measured current density−voltage (*J*−*V*) characteristics of the GaAs p−i−n NP-array solar cells under AM1.5G. (b) Calculated *J*−*V* curve by means of finite-difference time-domain simulations.

morphology of the ITO layer is dependent on the height of etched back NP tip as presented in Figure S3 (Supporting Information). A thin titanium interlayer is found to improve the ohmic behavior at the ITO/p-GaAs interface after rapid thermal annealing. Figure 2c plots the apparent photocurrent as a function of increasing areas. The measurements reveal a linear dependence with respect to the number of NPs contacted which are indeed responsible for the collective photovoltaic response of the devices. Nonetheless, the linear regression intercepts the *y*-axis at $I_{\mathrm{PH,SUB}}$ = 3.2 μA for a zero projected active area. This result quantifies a parasitic photocurrent presumably generated by the semiconductor substrate under AM1.5G illumination (see Supporting Information). The actual photocurrent values delivered by the NP solar cells can be extrapolated by rigidly translating downward the linear curve to intercept the origin. Subsequent to the correction for the substrate baseline, an area-independent plot of the actual photocurrent density can be formalized as presented in Figure 2d.

Core-multishell NP-array photovoltaic devices are tested both under dark and under AM1.5G conditions. In the dark, the ideality factor of the GaAs p−i−n NP-array is 1.86, whereas the rectification ratio at ±1 V is $>10^5$. Reverse-bias leakage currents of 48 nA at −1 V indicate a high quality material, where the detrimental effect of surface states is moderated by capping the active region with a thin, lattice-matched, high bandgap InGaP shell.[21] Under illumination, open-circuit voltages (V_{OC}) of 0.57 V, short-circuit photocurrent densities (J_{SC}) of 18.9 mA/cm^2 with fill factors (FF) up to 69% are observed as shown in the *J*−*V* characteristic of Figure 3a. The resulting power conversion efficiency (PCE) of η = 7.43% represents a considerable improvement with respect to previous reports for GaAs NP-array photovoltaics. The measured PCE considers the sole photocurrent contribution generated in the NP-array. So far, GaAs-based epitaxial NW solar cells have been affected by low V_{OC} values ranging from 0.2[9] to 0.24 V,[24] without the adoption of any passivation scheme and depending on the different growth method. Part of the reason is related to the large surface-to-volume ratio involved in NP-based photovoltaics. Since the active junction increases as well as surface/interface recombination rates, InGaP window layers demonstrated to reduce the surface recombination in planar GaAs solar cells.[21] To gain insight on the electronic transport under AM1.5G, FDTD, and electrical simulations are carried out using Sentaurus TCAD software suite. The FDTD method has been widely adopted in optoelectronic modeling of NPs, enabling the analysis of subwavelength light trapping mechanisms in a wave optics framework.

Figure 3b displays the calculated *J*−*V* characteristics under light, introducing a residual surface state density $N_{\mathrm{S}} = 1 \times 10^{10}$ eV^{-1} cm^{-2}. The major V_{OC} improvement compared to previous NP reports[9,24] can be attributed to both the epitaxial windows as well as the p−i−n junction design. In fact, p−i−n junction schemes have demonstrated higher V_{OC} compared to p−n core−shell structures[7] due to a decreased dark saturation current, for NW diameters as low as 200 nm. Nonetheless, incomplete Fermi level unpinning at the surface is responsible for a lower V_{OC} with respect to planar photovoltaics, attributed in part to a nonideal passivation. This leads to a remainder surface recombination velocity $S_{\mathrm{PASS}} = 10^4$ cm/s after passivation (see Supporting Information). Additionally, a complete array of NWs offers a route to large area integrations, however, is much more sensitive to variations compared to single-NW photovoltaics: defective NPs across the whole array can directly reduce the device shunt resistance. The V_{OC} of NW solar cells is an ensamble measurement of millions of miniaturized p−n junctions connected in parallel between anode and cathode, and slight variations in the electrical properties of each single NP (e.g., shunt resistance, built-in electric field, ideality factor) may severely affect the overall *J*−*V* characteristics.

Figure 4 displays the EQE of the corresponding photovoltaic NP devices. The experimental spectral data (blue dots), taken from 400 to 950 nm wavelength, shows maximum EQE values of ~70%, with an average magnitude $\mathrm{EQE}_{\mathrm{AVE}} > 60\%$. Several peaks can be noticed at different wavelengths which can be attributed to the confinement/localization of guided modes within the NP-array. As presented in Figure 2b, the overlaid ITO electrode naturally assumes a dome-shaped morphology on top the NPs due to the conformal type of deposition. The particularly rounded geometry occurs from the high nearest-neighbor interaction of the sputtering plasma among NPs in the highly packed array. The self-constituted nanostructured ITO layer has been reported to have excellent light trapping capabilities due to its unique nanophotonic effects.[25,26] Nonetheless, a high-efficiency photovoltaic device is characterized not only by enhanced solar absorption but also a remarkable collection of photocarriers which requires coupling of both optical and electrical modeling. In order to calculate the

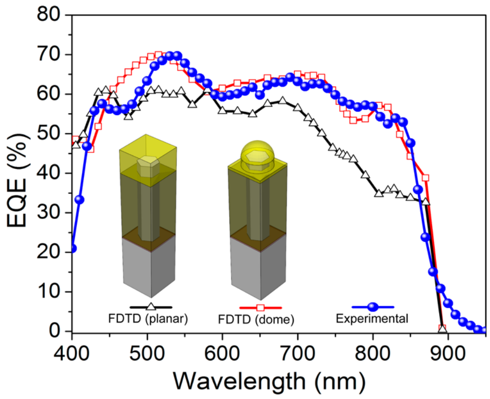

Figure 4. External quantum efficiency measurements (blue dots) of the solar cells from 400 to 950 nm. FDTD simulations are carried out to analyze the impact of a planar (black triangles) and a dome-shaped ITO layer (red squares) on the final optical coupling performance. The latter shows a good fidelity compared to the measured data.

optical generation rate G_{ph}, the Poynting vector S is defined in the form of

$$G_{ph} = \frac{|\vec{\nabla}\cdot\vec{S}|}{2\hbar\omega} = \frac{\varepsilon''|\vec{E}|^2}{2\hbar}$$

where ω is the frequency of the incident light, $\hbar$ is the reduced Planck's contact, E is the electric field intensity at each grid point, and ε'' is the imaginary part of the permittivity. For the electrical modeling, optical generation profiles are first interpolated automatically to the finite-element mesh of the NWs, and then a coupled set of Poisson equation and carrier continuity equations are solved for each meshing point to compute the photocurrent at every single wavelength.

The resulting simulations (red squares and black triangles) are presented in Figure 4 and directly compared to the experimental data (blue dots). The EQE curves are found to be in good agreement within most of the wavelength range of interest (400–900 nm). The two peaks located at λ = 520 nm and λ = 810 nm are caused by Mie resonance[27,28] that leads to a highly effective coupling of incident light into the dome-shape ITO that through a leaky channel is funneled into the NPs. Conversely, the simulated EQE curve with planar ITO shows no significant peaks at the aforementioned wavelengths. This is inherent to the fact that planar ITO only functions as a common antireflective coating (ARC), whereas the dome-shaped ITO creates a graded effective refractive index profile between air and the NP, attenuating the surface reflection in a broad range of spectrum.[28] In the long wavelength range (λ > 700 nm), the EQE values of the structure with planar ITO drops dramatically as the incident light is less confined inside the NPs and more dissipated to the substrate with the absence of the dome-shaped ITO (see Supporting Information).

By accurately reproducing in the FDTD simulations both magnitudes and wavelengths of the measured EQE peaks, it is possible to consolidate a clear optical spectral analysis of the integrated NP photovoltaic devices. Figure 5a displays vertical cross sections of optical generation profiles through the center of the NP. Six different wavelengths are outlined: 405, 505, 600, 700, 808, and 892 nm. At λ = 405 nm where the absorption length of GaAs is fairly short, the majority of the photocarriers are generated at the surface of the NP, being the most sensitive to surface recombination and thus resulting in a relatively lower measured EQE. At longer wavelengths, the optical field is penetrating deeper into the internal part of the NP, generating electron–hole pairs more evenly distributed along the core–multishell structure. This is witnessed by higher EQE values. Due to the fact that the NP size is comparable to the wavelength,[29] a higher portion of the carriers is generated where the constructive interference of light takes place. The nanostructured ITO efficiently concentrates the light from the top portion of the NP. As a consequence, the photogeneration rate is greatly increased. In other words, the dome-shaped ITO acts as a nanolens layer on top of the NP-array, where the effective focal point is wavelength-dependent: the high optical generation region (red lobes) originating from the top of the NP migrates into the NP body for increasing wavelengths, as revealed by Figure 5a. Notably, these results demonstrate the confinement of light into nanoscale volumes, with minimal photogeneration located at the substrate. Reducing the amount of the active absorber represents a unique advantage of nanostructures, enabling practical low-cost photovoltaics. This demonstrates the capability to recycle the substrate for consecutive growths, further reducing production costs. Figure 5b exhibits a 3-D power flux density map of a 4-by-4 array of NPs under AM1.5G, with the front row cut away from the middle of the structure. The figure confirms the coupling of

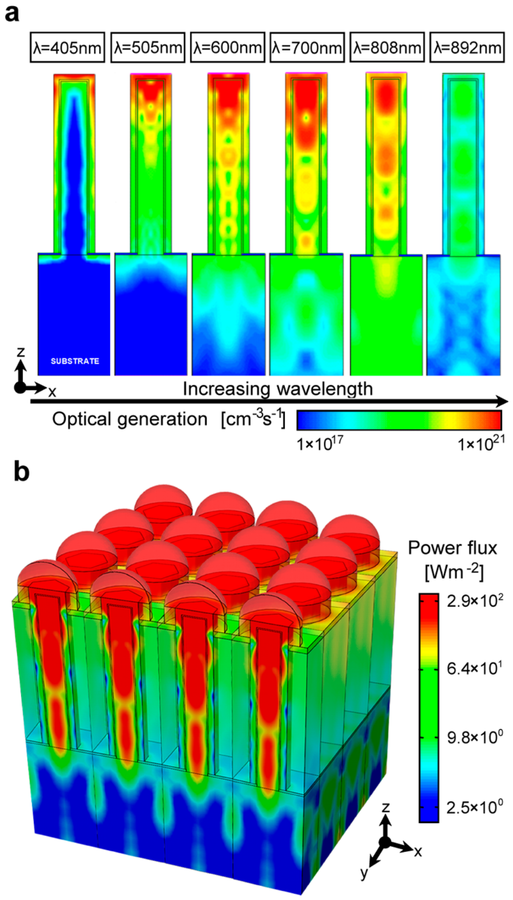

Figure 5. (a) Optical generation profiles calculated by FDTD for wavelengths at 405, 505, 600, 700, 808, and 892 nm. Color map is common to all six profiles. Through the dome-shaped ITO, the light is coupled into the NP-array, penetrating deeper into the semiconductor material at longer wavelengths. (b) Integrated-AM1.5G optical power flux within the periodic structure. Each ITO dome acts as a subwavelength nanolens, concentrating the optical power in the active NP region.

incident light into a 2-D array of nanolenses and subsequently into the whole NP array. A large portion of the power density is concentrated within the NP, leading to an increased local density of optical states. The map is calculated considering a solar-spectrum-weighted incident power, where both subwavelength effects from an infinitely periodic NP array and a dome-shaped ITO array are synergistically modeled.

In conclusion, this work presents 7.43%-AM1.5G efficiencies for periodic arrays of GaAs core-multishell NP solar cells and correlates *J*−*V* and EQE measurements with FDTD simulations for a full-wave optoelectronic analysis of the devices. Area-dependent photocurrent characterization quantifies substrate current contributions that could lead to an overestimation of short-circuit current densities in NP-based solar cells. *J*−*V* calculations highlight a residual surface state density $N_T = 1 \times 10^{10}$ eV^{-1} cm^{-2} after epitaxial passivation. Full-wave calculations fit with good fidelity the EQE experimental data and allow to extract realistic photogeneration profiles and delve into the spectral behavior of the fully integrated NP photovoltaic device. High optical absorption arising from the NP matrix is a necessary but not sufficient condition to achieve high-efficiency NP-based photovoltaics: cohesive optical and electrical investigation of the complete solar cells is paramount to correlate theoretical calculations with experimental results. This study demonstrates that epitaxial window layers are necessary to reduce surface recombination and the dome-shape of the nanostructured ITO layer can greatly foster the light coupling within the periodic NP array with respect to flat ARC depositions. The confinement of optical power flux inside the nanostructures effectively reduces the amount of active absorber with respect to thin-film architectures, enabling substrate recycling for practical low-cost photovoltaics.

Nanopillar Growth. The growth of the GaAs nanopillar arrays is achieved using a vertical-flow metal organic chemical vapor deposition chamber. N-doped GaAs cores are grown at 730C for 15 min; the intrinsic GaAs regions are synthesized at 600C for 1 min, and the p-doped shells are grown for 5 min at 600C. Lastly, the InGaP window layer is grown for 45 s at 600C. Dimethylzinc and tetraethyltin are used as p- and n-dopants, respectively.

Device Fabrication and Characterization. After epitaxy, all samples undergo an acetone−methanol−isopropanol rinse for 1 min. Acqueous solution of ammonium hydroxide (dilution ratio 30:1, H_2O/NH_4OH) is utilized to remove any native oxide at room temperature for 30s. Bottom ohmic contacts (Ge(5 nm)/Ni(10 nm)/Ge(15 nm)/Au(200 nm)) are deposited by e-beam evaporation and annealed rapidly at 380C for 1 min. Benzocyclobutene (BCB, Dow Chemical) is spin-coated, hard-cured, and etched back by reactive-ion etching (O_2/CF_4) to expose the top portion of the nanopillars. Standard photolithography is used to pattern the area-dependent contacts with increasing areas. Transparent contacts are deposited by radio frequency sputtering at 300W for 40 min, in an Ar/O_2 environment. *J*−*V* characteristics are acquired using a source meter (Keithley 2400). AM1.5 global (AM1.5G) illumination is achieved with a solar simulator equipped with a 300 W xenon-bulb (Newport 67005), a diffuser, and AM1.5G filter to smoothen any lamp peak. The AM1.5G illumination spot diameter is ∼33 mm on the device positioning stage. The external quantum efficiency (EQE) spectra are recorded using a manufactured EQE setup (Newport 74125) which includes a monochromator, lock-in amplifier, and calibrated silicon photodiode. A 100-mm-focal length objective lens is used to concentrate the spot size.

Finite-Difference Time Domain Simulations. Optoelectronic simulations are calculated using finite-difference time-domain (FDTD) methods (Sentaurus TCA, Synopsys Inc.). For the optical modeling, a Sentaurus electromagnetic wave solver (EMW) is used to perform FDTD calculations. Wavelength-dependent optical constants (refractive indices n and extinction coefficients κ) of GaAs and ITO are adopted from previous works,[30,31] whereas the refractive index of BCB is set constant at $n = 1.54$. To simulate the whole NP array, periodic boundary conditions are set on the side of the as-built structure, while Higdon absorbing boundary conditions are imposed at the top and the bottom of the structure.[32,33] Normally incident light is defined with power intensity and wavelength values from a discretized AM 1.5G solar spectrum. The corresponding unpolarized signature is achieved by superimposing the transverse electric (TE) and transverse magnetic (TM) mode contributions. For the electrical modeling, first the optical generation profiles are interpolated automatically to the finite-element mesh of the nanopillars, and then a coupled equation set of Poisson equation and carrier continuity equations are solved for each mesh point with specific boundary conditions to get the photocurrent at each wavelength. The Shockley−Read−Hall recombination, Auger recombination, and radiative recombination are all considered, while the carrier mobility is set to be doping-dependent.[3] Ideal ohmic contacts are defined both at the tip of the nanowire and the bottom of the substrate.

■ ASSOCIATED CONTENT

Ⓢ Supporting Information

Recombination model adopted in FDTD simulations, *J*−*V* comparison of simulated planar ITO and dome-shaped ITO, photocurrent contributions from area-dependent measurements, experimental EQE comparison between dome-shaped and planar ITO, Figures S1−S4. This material is available free of charge via the Internet at http://pubs.acs.org.

■ AUTHOR INFORMATION

Corresponding Author

*E-mail address: giacomomariani@ucla.edu.

Notes

The authors declare no competing financial interest.

■ ACKNOWLEDGMENTS

The authors gratefully acknowledge support from Air Force Office of Scientific Research (Grant No. FA-9550-12-1-0052), the National Science Foundation (Grant No. ECCS-1202591, Grant No. DMR-1007051), and the United States Department of Defense (Grant No. NSSEFF N00244-09-1-0091).

■ REFERENCES

(1) Greytak, A. B.; Barrelet, C. J.; Li, Y.; Lieber, C. M. *Appl. Phys. Lett.* **2005**, *87*, 151103.

(2) Huang, M. H.; Mao, S.; Feick, H.; Yan, H.; Wu, Y.; Kind, H.; Weber, E.; Russo, R.; Yang, P. *Science* **2001**, *292*, 1897−1899.

(3) Fan, Z.; Ho, J. C.; Jacobson, A. Z.; Razavi, H.; Javey, A. *Proc. Natl. Acad. Sci. U.S.A.* **2008**, *105*, 11066−11070.

(4) Hayden, O.; Agarwal, R.; Lieber, C. M. *Nat. Mater.* **2006**, *5*, 352−356.

(5) Bulgarini, G.; Reimer, M.; Hocevar, M.; Bakkers, E.; Kouwenhoven, L.; Zwiller, V. *Nat. Photonics* **2012**, *6*, 455−458.

(6) Goto, H.; Nosaki; Tomioka, K.; Hara, S.; Hiruma, K.; Motohisa, J.; Hukui, T. *Appl. Phys. Exp.* **2009**, *2*, 035004.
(7) Kempa, T. J.; Cahoon, J. F.; Kim, S.-K.; Day, R. W.; Bell, D. C.; Park, H.-G.; Lieber, C. M. *Proc. Natl. Acad. Sci. U.S.A.* **2012**, *109*, 1409−1412.
(8) Tang, J.; Huo, Z.; Brittman, S.; Gao, H.; Yang, P. *Nat. Nanotechnol.* **2011**, *6*, 568−572.
(9) Czaban, J. A.; Thompson, D. A.; LaPierre, R. R. *Nano Lett.* **2009**, *9*, 148−154.
(10) Cao, L.; White, J.; Park, J.-S.; Schuller, J. A.; Clemens, B. M.; Brongersma, M. L. *Nat. Mater.* **2009**, *8*, 643−646.
(11) Kayes, B.; Atwater, H. *J. Appl. Phys.* **2005**, *97*, 114302.
(12) Tsakalakos, L.; Balch, J.; Fronheiser, J.; Korevaar, B. A. *Appl. Phys. Lett.* **2007**, *91*, 233117.
(13) Wei, W.; Bao, X.; Soci, C.; Ding, Y.; Wang, Z.; Wang, D. *Nano Lett.* **2009**, *9*, 2926−2934.
(14) Chen, R.; Tran, T.-T.; Ng, K.; Ko, W. S.; Chuang, L.; Sedgwick, F.; Chang-Hasnain, C. *Nat. Photonics* **2011**, *5*, 170−175.
(15) Weisse, J.; Lee, C.; Kim, D.; Zheng, X. *Nano Lett.* **2012**, *12*, 3339−3343.
(16) Kosten, E.; Warren, E.; Atwater, H. *Opt. Express* **2011**, *4*, 3316−3331.
(17) Wen, L.; Zhao, Z.; Li, X.; Shen, Y.; Guo, H.; Wang, Y. *Appl. Phys. Lett.* **2011**, *99*, 143116.
(18) Kailuweit, P.; Peters, M.; Leene, J.; Mergenthaler, K.; Dimroth, F.; Bett, A. *Prog. Photovolt: Res. Appl.* **2011**, DOI: 10.1002/pip.1169.
(19) Wu, P.; Anttu, N.; Xu, H.; Samuelson, L.; Pistol, M.-E. *Nano Lett.* **2012**, *12*, 1990−1995.
(20) Shapiro, J.; Lin, A.; Scofield, A.; Tu, C.; Wong, P.-S.; Senanayake, P.; Mariani, G.; Liang, B. L.; Huffaker, D. L. *Appl. Phys. Lett.* **2010**, *97*, 243102.
(21) Plá, J.; Barrera, M.; Rubinelli, F. *Semicond. Sci. Technol.* **2007**, *22*, 1122−1130.
(22) Muralidharan, E.; Ploog, K. *Appl. Phys. A: Mater. Sci. Process.* **1989**, *49*, 527−531.
(23) Loferski, J., Roessler, B., Crisman, E., Chen, Y., Kaul, L., Walker, J. *NASA Ninth semiannual report*; Brown University: Providence, RI, 1974.
(24) Cirlin, G.; Bouravleuv, A.; Soshnikov, I.; Samsonenko, Y.; Dubrovskii, V.; Arakcheeva, E.; Tanklevskaya, E.; Werner, P. *Nano. Res. Lett.* **2010**, *5*, 360−363.
(25) Ferry, V. E.; Polman, A.; Atwater, H. A. *ACS Nano* **2011**, *11*, 10055−10064.
(26) Zhu, J.; Hsu, C.-M.; Yu, Z.; Fan, S.; Cui, Y. *Nano Lett.* **2010**, *10*, 1979−1984.
(27) Spinelli, P.; Verschuuren, M. A.; Polman, A. *Nat. Commun.* **2012**, *3*, 692−696.
(28) Leem, J. W.; Yu, J. S. *Opt. Express* **2012**, *20*, A431−A440.
(29) Li, J.; Yu, H.; Li, Y. *Nanotechnology* **2012**, *23*, 194010.
(30) Palik, E. D. *Handbook of Optical Constants Solids*; Academic Press: New Yorkm 1985.
(31) http://homepages.rpi.edu/~schubert/Educational-resources/Materials-Refractive-index-and- extinction-coefficient.pdf.
(32) Higdon, R. L. *Math. Comput.* **1986**, *47*, 437−459.
(33) Synopsys Inc. *Sentaurus TCAD User Guide*, Version E-2010.12; Synopsys Inc.: Switzerland, 2010.